JOURNAL OF GEOPHYSICAL RESEARCH: SPACE PHYSICS, VOL. 118, 232–243, doi:10.1029/2012JA017998, 2013

POES satellite observations of EMIC-wave driven relativistic electron precipitation during 1998–2010

Bonar R. Carson,[1] Craig J. Rodger,[1] and Mark A. Clilverd[2]

Received 4 June 2012; revised 4 November 2012; accepted 16 November 2012; published 31 January 2013.

[1] Using six Polar Orbiting Environmental Satellites (POES) satellites that have carried the Space Environment Module-2 instrument package, a total of 436,422 individual half-orbits between 1998 and 2010 were inspected by an automatic detection algorithm searching for electromagnetic ion cyclotron (EMIC) driven relativistic electron precipitation (REP). The algorithm searched for one of the key characteristics of EMIC-driven REP, identified as the simultaneity between spikes in the P1 (52 keV differential proton flux channel) and P6 (>800 keV electron channel). In all, 2331 proton precipitation associated REP (PPAREP) events were identified. The majority of events were observed at L-values within the outer radiation belt ($3 < L < 7$) and were more common in the dusk and night sectors as determined by magnetic local time. The majority of events occurred outside the plasmasphere, at L-values ~1 R_e greater than the plasmapause location determined from two different statistical models. The events make up a subset of EMIC-driven proton spikes investigated by Sandanger *et al*. (2009), and potentially reflect different overall characteristics compared with proton spikes, particularly when comparing their location to that of the plasmapause, i.e., EMIC-driven proton precipitation inside the plasmapause, and potentially EMIC-driven REP outside the plasmapause. There was no clear relationship between the location of plasmaspheric plumes and the locations of the PPAREP events detected. Analysis of the PPAREP event occurrence indicates that high solar wind speed and high geomagnetic activity levels increase the likelihood of an event being detected. The peak PPAREP event occurrence was during the declining phase of solar cycle 23, consistent with the 2003 maximum in the geomagnetic activity index, *Ap*.

Citation: Carson, B. R., C. J. Rodger, and M. A. Clilverd (2012), POES satellite observations of EMIC-wave driven relativistic electron precipitation during 1998–2010, *J. Geophys. Res. Space Physics*, *118*, 232–243, doi:10.1029/2012JA017998.

1. Introduction

[2] Since their discovery in 1958, the Van Allen Radiation Belts have been an area of intense interest and research. The complex nature of the belts and the interactions that occur within them mean there is no easy solution to many of the fundamental questions concerning the radiation belts. Indeed, even similar geomagnetic storms can produce different results in terms of enhancing or depleting radiation belt particle populations [*Reeves et al*., 2003]. Spacecraft that fly through these belts are at risk of damage, and for manned spacecraft the radiation poses a health risk to astronauts. The interactions of the belts with the Earth's atmosphere, through the precipitation of particles, affect atmospheric chemistry and can include the destruction of mesospheric and stratospheric ozone [*Brasseur and Solomon*, 2005]. One depletion process involves the interaction of electrons with electromagnetic ion cyclotron (EMIC) mode waves in the inner magnetosphere.

[3] Recently, studies have provided evidence linking specific events of observed precipitation of relativistic electrons with simultaneous observations of EMIC waves [*Rodger et al*., 2008; *Miyoshi et al*., 2008]. EMIC waves are the highest frequency electromagnetic waves in the ULF spectral regime. They are observed in ground-based observations as Pc 1–2 (0.1–5 Hz) waves and sometimes extend to frequencies above 5 Hz in space-based observations [*Fraser et al*., 2006]. One of the most comprehensive satellite missions that examined EMIC wave occurrence was provided by the AMPTE mission [e.g., *Anderson et al*., 1992; Anderson, 1995], which showed that EMIC waves preferentially occur on the dayside and afternoon/dusk sector. In contrast, *Meredith et al*. [2003] conducted a statistical study of more than 800 EMIC wave events and found that the majority occurred on the duskside of the magnetosphere (1300 < magnetic local time (MLT) < 2000) for $L > 3$, as seen in Figure 3 of their study, although this may have been an

[1]Department of Physics, University of Otago, Dunedin, New Zealand.
[2]British Antarctic Survey (NERC), High Cross, Madingley Road, Cambridge, England, United Kingdom.

Corresponding author: C. J. Rodger, Department of Physics, University of Otago, P.O. Box 56, Dunedin, New Zealand. (crodger@physics.otago.ac.nz)

2169-9380/13/2012JA017998

Table 1. Detectors That are Part of the POES Space Environment Monitor-2 (SEM-2) Package Used in the Current Study[a]

Data Channel	Observes	Directionality	Accumulation Period
E2	>100 keV e^-	0°, 90°	1 s
P1	52 keV diff. p^+	0°, 90°	1 s
P5	2628 keV diff. p^+	0°, 90°	1 s
P6	>6.9 MeV p^+	0°, 90°	1 s
$P6_{omni}$	>16 MeV p^+	0°	2 s

[a]The telescopes viewing 0° and 90° are ±15° wide, while the omnidirectional detectors (labeled "omni") are ±60° wide. The nature of the relativistic electron contamination for the P6 and $P6_{omni}$ detectors is described in *Yando et al.* [2011].

artefact of the CRRES mission ending before it could complete a full precession around the Earth, missing the region where the majority of EMIC waves were seen in the AMPTE observations. Preferential regions for EMIC wave generation can include the dayside sector during enhanced solar wind density and related magnetic compressions [*Usanova et al*., 2008], close to the plasmapause in the nightside sector [*Pickett et al*., 2010], and in dayside plasmaspheric plumes [*Fraser et al*., 2005; *Fraser et al*., 2010]. *Fraser and Nguyen* [2001] have observed waves both inside and outside the plasmapause, with a slight enhancement of wave power at the plasmapause itself.

[4] EMIC waves are believed to be generated through unstable ring current ion distributions [*Cornwall*, 1965] and generated primarily in the equatorial region of the magnetosphere [*Anderson et al*., 1992]. Their source region is also observed to extend to lower *L*-values with increasing storm intensity [*Bortnik et al*., 2008]. *Halford et al*. [2010] used their statistical observations to characterize the mean EMIC location as $L = 5.83$ and MLT = 15.38 h, i.e., close to the expected location of a plasmaspheric plume or the plasmapause given the current geomagnetic conditions. EMIC waves are significantly more likely to occur during geomagnetic storms, with the largest amplitude waves occurring in the duskside sector [*Erlandson and Ukhorskiy*, 2001]. Spacecraft have shown that while waves occur during the recovery phase, the peak occurrence rate is during the main phase of the storm [*Halford et al*., 2010]. However, ground-based observations have a different pattern, with the waves mainly observed during the recovery phase of the geomagnetic storms [*Engebretson et al*., 2008].

[5] Particle precipitation of radiation belt energetic and relativistic electrons and comparatively low-energy protons comes about through cyclotron resonant wave-particle interactions [e.g., *Tsurutani and Lakhina*, 1997]. For electrons, the dominant interaction tends to be with whistler mode waves, which are by definition right-hand polarized, for example chorus, hiss, or whistlers themselves. As protons have the opposite charge, these can interact with the left-hand polarized ion-cyclotron waves, one example of which are EMIC waves; in practice the frequency range of the EMIC waves limit them to precipitating ions with energies of tens of keV generating the proton aurora [*Jordanova et al*., 2007]. Both of these cyclotron interactions are termed "normal resonance", and involve counter-streaming particles and waves. Another possibility is "anomalous" cyclotron resonant interactions, where the particle overtakes the wave [*Tsurutani and Lakhina*, 1997]. It has been known since the 1970s that this resonance should allow the interaction of EMIC waves with relativistic electrons [e.g., *Lyons and Thorne*, 1972] resulting in pitch angle scattering into the bounce loss cone and thus precipitation, which can be calculated through theory [*Summers and Thorne*, 2003] and included in models [*Jordanova et al*., 2008]. Note however, that only relativistic energy electrons (~MeV) appear to be able to meet the anomalous resonance criteria [*Meredith et al*., 2003], as the lower energy limit for EMIC-electron interactions is normally larger than 2 MeV. Direct experimental evidence for the predicted link between EMIC waves and precipitating relativistic electrons took several decades to appear [*Rodger et al*.; 2008; *Miyoshi et al*., 2008]. A review of radiation belt relativistic electron losses has been produced by *Millan and Thorne* [2007].

[6] In this study we provide a comprehensive investigation into interactions between relativistic electrons and EMIC waves in the radiation belts. Whereas other studies have focused on a small number of storm events, this study investigates 12 yr worth of data from six polar orbiting satellites equipped with particle detectors (Polar Orbiting Environmental Satellites (POES) and Meteorological Operational (METOP-2)). The key signatures of the precipitation of relativistic electrons driven by EMIC waves are identified from the satellite particle data. A database of these precipitation events was generated using autodetection code written specifically for this study, searching the large volume of data available for the aforementioned key signatures. We perform a statistical analysis with the database, to identify the observational characteristics of the EMIC-driven relativistic electron precipitation events, and determine their occurrence relationship with geomagnetic activity.

2. Instrumentation and Data

[7] Here we utilize the second-generation Space Environment Module (SEM-2) flown on the POES series of satellites, and on the METOP-02 spacecraft. For our study there are six satellites that carry on board the SEM-2 instrument package. The spacecraft are in Sun-synchronous polar orbits with typical parameters of ~800−850 km altitude, 102 min orbital period and 98.7° inclination [*Robel*, 2009]. The orbits typically are either morning or afternoon daytime equator crossings, with corresponding nighttime crossings. For this study we make use of all available data from when the individual satellites start operation to the end of 31 December 2010, a total of 15,441 days flown.

[8] The SEM-2 package includes the Medium Energy Proton and Electron Detector (MEPED), which was designed to monitor the intensities of protons and electrons over a range extending from 30 keV to greater than 200 MeV [*Evans and Greer*, 2000]. Table 1 lists the SEM-2 detectors used in the current study, where "E" refers to electron detectors and "P" proton detectors. It contains two pairs of directional telescopes and four omnidirectional detectors. The 0° (or vertical) telescopes are mounted so that the center of its field of view is looking outward along the local zenith, parallel to the Earth-center-to-satellite radial vector. The 90° (or horizontal) telescopes are approximately perpendicular to the 0° telescopes, looking antiparallel to the spacecrafts

direction of travel. The omnidirectional dome detectors are mounted parallel to the 0° telescopes. The POES spacecraft are three-axis stabilized such that their orientation is fixed with respect to their direction of travel; therefore, the detectors direction is consistent. The 0° and 90° telescopes are ±15° wide, while the omnidirectional dome detectors are ±60° wide. Each pair of directional telescopes includes an electron telescope designed to measure electrons between 30 keV and 2500 keV using three channels, and a proton telescope measuring protons from 30 keV to more than 200 MeV using six channels. The omnidirectional detectors provide a further four channels of proton detection for energies greater than 16 MeV.

[9] Data from the telescope channels is recorded every 2 s, with the recorded value being taken over a 1 s accumulation period. Accumulation is alternated between the two look directions, i.e., the 0° channels accumulate for 1 s, then the 90° channels accumulate for 1 s, giving a 2 s resolution for these channels but with alternating 1 s samples from each. The omnidirectional channel P6 also has a 2 s resolution; however, this utilizes an accumulation period of 2 s.

[10] *Rodger et al*. [2010a] has described what radiation belt population each of these telescopes samples for different locations. The 0° telescopes primarily measure in the bounce loss cone, with the only exception being close to the geomagnetic equator. Therefore, for all areas of interest in this study all 0° fluxes can be treated as sampling some fraction of the population of precipitating particles. However, the 90° telescopes measure a much more variable and complicated population. In particular, the region to the east of South America known as the South Atlantic Magnetic Anomaly (SAMA) includes high energy protons that reside in the inner radiation belt and affect the P6 channel, which would have serious implications for this study. As a result, all MEPED data within the SAMA are removed from further analysis to guarantee an uncontaminated data set. This is done by defining a lat-long range and removing all data in this area, with the spatial range defined by plotting the POES fluxes on a world map and conservatively setting a "SAMA region"; the limits of the SAMA region are shown shaded in Figure 2.

[11] Previous studies have made use of the fact that the P6 channel can be contaminated by relativistic electrons [e.g., *Miyoshi et al*., 2008; *Evans et al*., 2008; *Sandanger et al*., 2009; *Horne et al*., 2009; *Rodger et al*., 2010b; *Millan et al*., 2010] , and thus this channel can be used to monitor relativistic electron fluxes. The contamination is due to relativistic electrons having energies high enough to allow passage through the proton telescope without being deflected by the cross-aperture magnetic field and therefore can reach the detector stack. However, modeling by *Yando et al*. [2011] has shown that the P5 channel is immune to this contamination and therefore will only respond to protons. This allows the presence of relativistic electrons to be tested through comparison of the P6 channel with the P5 channel. This result allows us to utilize the MEPED P6 telescope channel as a relativistic electron detector in our study, as long as attention is paid to the corresponding P5 channel to ensure that it is only used as such in the absence of high energy protons. For this study we will consider the P6 channel to measure electrons with energies above about 800 keV, as this is when the geometric factor of the detector starts to reach a significant value.

[12] Note that *Yando et al*. [2011] also shows that relativistic electrons can contaminate the low energy MEPED proton channels, such that strong relativistic electron precipitation appearing in P6 can manifest as weak proton precipitation in P1 with about 10 times smaller counts.

3. Auto-Detection Algorithm

[13] In order to analyze the very large amount of data available from the satellites, an algorithm was developed to automatically detect likely EMIC-driven relativistic electron precipitation (REP). Other studies have reported a strong correlation between anisotropic proton precipitation and ground-based measurements of waves in the Pc1 frequency range [e.g., *Spasojevic and Fuselier*, 2009, and references therein]. *Søraas et al*. [2005] matched localized increases of relativistic electron flux to similar increases in low-energy proton flux, as measured by the MEPED P1 telescope (52 keV differential proton flux detector). *Sandanger et al*. [2007, 2009] then further matched these peaks in the relativistic electron and proton fluxes with corresponding research suggesting these structures to be the particle counterparts of EMIC.

[14] One of the key characteristics expected for EMIC-driven REP is the approximate simultaneity between the P1 (52 keV differential proton flux channel) and P6 (larger than about 800 keV electron channel) spikes in the 0° detectors. For this study, simultaneity was taken to be a P6 trigger occurring within ±4 data points of the location of a P1 trigger (i.e., ±8 s), where the triggering algorithm is described below. This "near simultaneous" window is used instead of exactly simultaneous as it is otherwise too restrictive, and this is consistent with *Imhof et al*. [1986] who allowed for potential displacements due to details of the plasma density profiles and the wave intensity-frequency distributions in this way. The detection algorithm followed this sequence:

[15] 1. Individual half orbits, from one pole to the opposite, are loaded. A running mean with a window of 30 s is applied to the 0° detector on both the P1 and P6 channels.

[16] 2. Any points where the actual measured value exceeds the running mean by a factor of 3 or more are noted as an event candidate.

[17] 3. Near simultaneous events in both P1 (52 keV differential proton flux) and P6 (electrons with energies larger than about 800 keV) channels are found, all other events are ignored.

[18] 4. Other aspects from the data are analyzed to determine if the events are likely to be a false detection (e.g., test for the presence of solar protons, crossing the SAMA boundary, or interference due to the weekly in-flight calibration events).

[19] 5. Only one event is allowed per hemisphere per half orbit.

[20] 6. The process is repeated for every half orbit available.

[21] An example of a half-orbit containing an event from 11:43–12:34 UT on 20 February 2009 is shown in Figure 1. From top to bottom the figures show: four telescope channels (P1, P6, P5, E2) in both look directions, 0° (blue lines) and 90° (red lines), and one omnidirectional channel ($P6_{omni}$), as well as the satellite ground track on a world map. The SAMA in

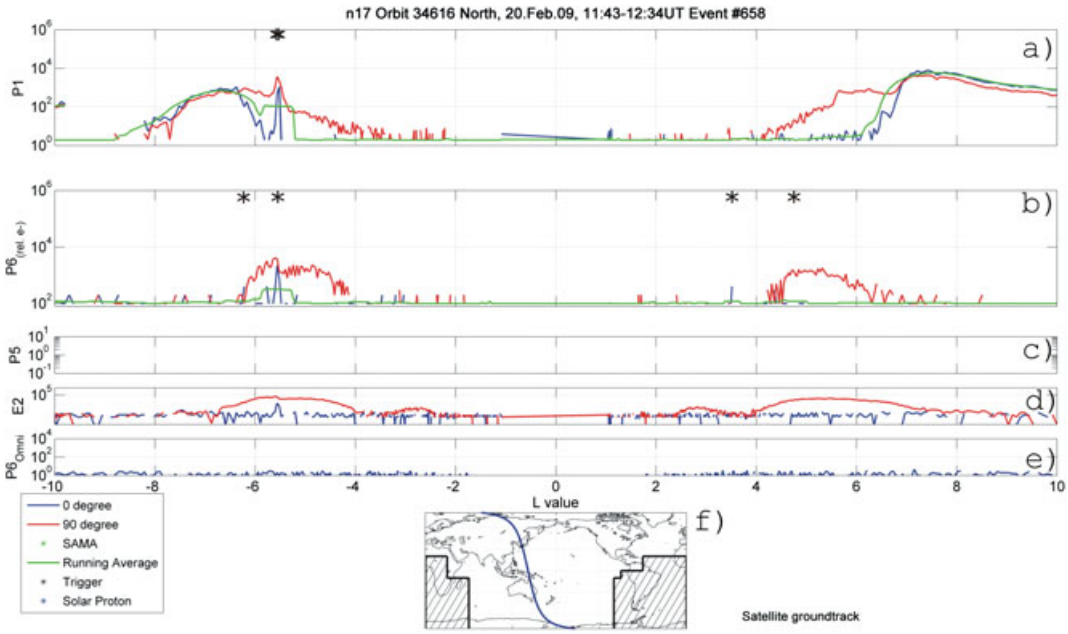

Figure 1. An example of a NOAA-17 event from 20 February 2009. From top to bottom the panels show: four telescope channels (P1, P6, P5, E2) in both look directions, 0° (blue lines) and 90° (red lines), and one omnidirectional channel ($P6_{omni}$), as well as the satellites ground track on a world map. The SAMA in the Southern Hemisphere is identified by shading, and no event detection within this region is undertaken. The running means that are calculated for the P1 0° channel and P6 0° channel are shown by green lines. The location of triggers identified with the autodetection algorithm are marked by a black asterisk in the upper two panels.

the Southern Hemisphere is identified by the shaded region, and no event detection within this region is undertaken. The running means that are calculated for the P1 0° channel and P6 0° channel are shown by green lines. The locations of triggers identified with the autodetection algorithm are marked by a black asterisk in Figures 1a and 1b. All detected triggers are included even if they did not lead to an event being defined. The coincidence of the event triggers in the P1 and P6 0° telescopes identifies an event occurring at $L \sim 5.5$ in the Southern Hemisphere, somewhere south of Australia/New Zealand. The P5 proton channel is presented in Figure 1c. This was included as it is used to check for solar proton contamination. As noted earlier, having the P5 channel visibly empty confirms that the P6 channel (Figure 1b) is measuring relativistic electrons and not high energy protons. In addition, as the P6 and P1 channels have similar fluxes we can rule out the P1 response being solely due to the presence of relativistic electrons. Figures 1e and 1f are included solely for quick reference as to what else is happening during these events. The E2 >100 keV electron telescope observations in Figure 1d suggest that the event identified by the P1 and P6 data (Figures 1a and 1b) has a small response at nonrelativistic electron energies, as expected for resonance with EMIC waves [e.g., *Meredith et al*., 2003]. Figure 1e shows the lowest energy omnidirectional channel ($P6_{omni}$), which *Miyoshi et al*. [2008] suggested can also be used to detect the presence of precipitating relativistic electrons, although this is not used as part of the automatic detection algorithm presented here.

[22] A database of all detected events was generated in order to allow mass statistical analysis to be performed. A total of 436,422 individual half orbits were inspected using the automatic algorithm. The database contains 2331 events from all six satellites covering the period from 1 July 1998 to 31 December 2010. The statistics for each individual satellite can be seen in Table 2, which includes the date after which the satellite data became available. All satellites listed continue to function as of 27 July 2012. As these events were found by searching for the expected particle precipitation signature created by scattering due to EMIC waves, but

Table 2. Total Half Orbits Inspected and Events Detected by Each Individual Satellite[a]

Satellite	Data Availability	Half-orbits Inspected	Events Detected	Event Detection %
NOAA-15	1 July 2008	129,259	602	0.47
NOAA-16	10 January 2001	102,490	625	0.61
NOAA-17	12 July 2002	87,848	704	0.80
NOAA-18	7 June 2005	57,047	189	0.33
METOP-02	3 December 2006	40,932	178	0.43
NOAA-19	23 February 2009	18,846	33	0.18
Total		436,422	2,331	0.53

[a]Satellites are listed in order of launch.

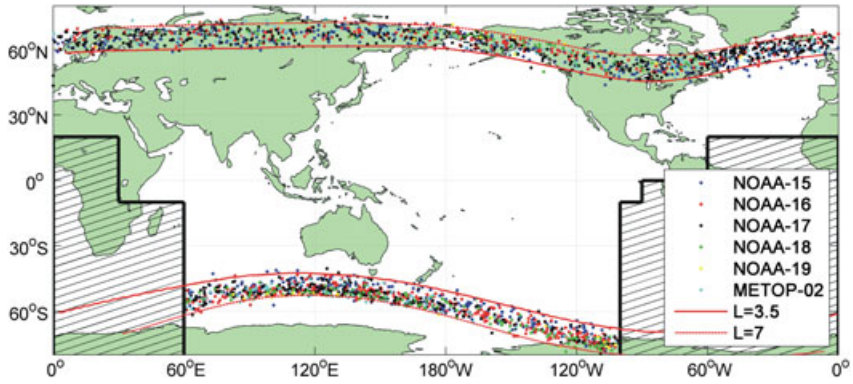

Figure 2. A map of the subsatellite locations of the detected events. Each event is color coded to identify the satellite from which it was detected. The hashed region represents the area of the SAMA where analysis of data is not undertaken. Red lines mark the IGRF L-shells $L = 3.5$ (solid) and $L = 7$ (dashed) as calculated at the satellite altitude.

as no EMIC wave observations were available to confirm this, we term the events "proton precipitation associated REP" (PPAREP) events. An estimate of the event detection percentage for each individual satellite is made by taking the ratio of the number of half-orbits inspected by the number of events detected. It is apparent that not all satellites had the same rate of event detection, probably due to a number of circumstances, including different MLT orbital patterns and also the influence of differing geomagnetic conditions within each satellite operational window. However, typically ~0.5% of half-orbits contained a PPAREP event. In the next section we investigate the observational characteristics of the PPAREP events, and determine their occurrence relationship with parameters such as indexes of geomagnetic activity.

4. Results

[23] A geographical world map identifying the subsatellite location of all 2331 events is shown in Figure 2. Each PPAREP event is color-coded to identify the satellite from which it was detected. The hashed region represents the area of the SAMA where analysis of data is not undertaken. Red lines mark the International Geomagnetic Reference Field (IGRF) L-shells $L = 3.5$ (solid) and $L = 7$ (dashed) as calculated at the satellite altitude. This figure indicates that the PPAREP events show a geomagnetic occurrence distribution linked to L-shells. Detailed analysis indicates that the events occur over a range of L-shell values, with a minimum of $L = 2.87$ and a maximum of $L = 9.93$, although the upper limit here will come from the maximum L-value possible in the triggering algorithm ($L = 10$), chosen due to the very high variability and associated false trigger rate over the poles.

[24] Figure 3 (top) shows the histogram of events sorted by IGRF L-value, with a bin width of 0.5 L. 94% of all of the events are contained within the range $3.5 < L < 7$ shown. Figure 3 (middle) shows the normal background frequency of the satellite observations within each L-value bin, i.e., all 2 s resolution L-values. The satellites tend to spend longer periods of time within lower L-values due to the way the L-shell separation increases with decreasing L-shell; this is reflected in the way the frequency decreases at higher L-values in this figure. Figure 3 (bottom) shows the normalized result of the frequency of events by L-value with the bias of satellites spending more time at lower L-shells removed. In this case the normalization process correcting this bias does very little to the overall trend; the bins at lower L-values are lowered slightly in comparison with the raw counts shown in Figure 3 (top); however, the event distribution is still centered around $L = 5.25$.

[25] In order to look for signs of MLT dependence we sum across all L-values for a given MLT bin. Figure 4 (top panel) shows the results of this summation, indicating a very strong MLT dependence in the raw event timing, with a factor of approximately 60 between the highest and lowest frequency bins. Occurrence frequency values during 04−16 MLT are lower overall compared with 16−04 MLT. However, this variation is potentially biased by the uneven MLT coverage of the satellite observations. In the middle panel we can see how the combination of all six satellites provides good coverage of all MLTs, and there is only a range of approximately a factor of two in the counts between the lowest and highest frequency MLT bins. Finally, the bottom panel

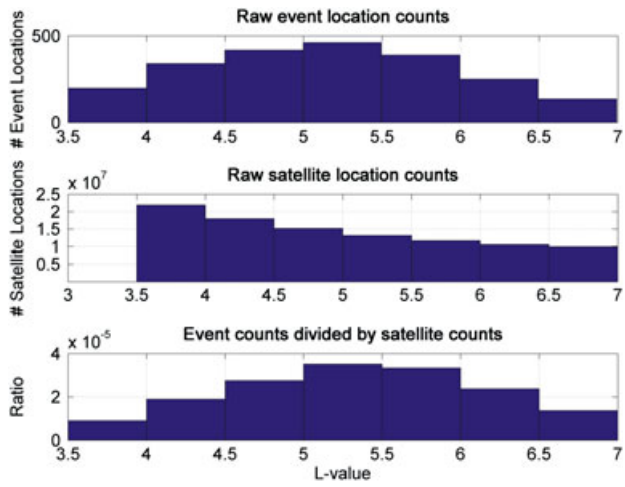

Figure 3. (top) A histogram of events sorted by IGRF L-value, with a bin width of 0.5 L. (middle) The normal background frequency of the satellite observations within each L-value bin. (bottom) The normalized distribution of the REP events sorted by L-value.

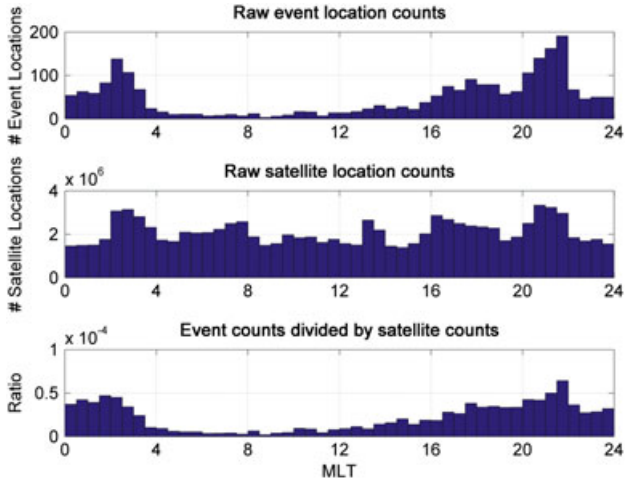

Figure 4. (top) The raw MLT distribution of events, indicating a very strong MLT dependence, with a factor of approximately 60 between the highest and lowest frequency bins. (middle) The combination of all six satellites provides good coverage of all MLTs, and there is only a range of approximately a factor of two in the counts between the lowest and highest frequency MLT bins. (bottom) The normalized frequency of events by MLT after being adjusted for satellite observational bias.

gives the true frequency of events by MLT after being adjusted for satellite bias. The range between the highest and lowest event observations has now decreased to a factor of approximately 30, with the significant increase across 16−04 MLT remaining. The MLT range 16−04 corresponds with the dusk and night sectors. The frequency distribution shows a double peak, with one peak at 22 MLT and the other at 02 MLT.

[26] In order to investigate the *L*-shell and MLT dependence of the detected events more closely, Figure 5 shows the distribution of *L*-value and MLT in a clock-plot, where *L*-value increases from 0–7 R_e outward from the center, and MLT rotating anticlockwise with 12 MLT (noon) at the top, and 00 MLT (midnight) at the bottom. The plot shows two clusters of occurrence, one before and one after 00 MLT. The 00–04 MLT cluster appears very clearly, has the highest occurrence frequency values in the plot, and is centered on $L \sim 6$. The 16–22 MLT cluster has lower occurrence frequency, and is centered on $L \sim 5$. There is no cluster of events on the dayside (12–18 MLT), which would correspond to the high *L*-shell region of EMIC waves that occur within plasmaspheric plume structures [*Fraser and Nguyen*, 2001; *Fraser et al*., 2005; *Darrouzet et al*., 2008]. Our finding is consistent with the report of *Posch et al*. [2010] who using ground-based data saw little overlap of EMIC wave occurrence location and plasmaspheric plumes observed in space, although their result may be affected by poor propagation conditions for EMIC waves to the ground during storms.

[27] The majority of satellite observations were made during quiet geomagnetic conditions, with the most common *Kp* value being 0.3–0.7 and *Dst* of –5 nT, although it is generally expected that more precipitation will occur during disturbed conditions. In order to test the dependence of our 2331 PPAREP events on geomagnetic and solar wind conditions, we associate a geophysical parameter with each half-orbit (as outlined below) and then compare the occurrence rate of our PPAREP events for a given geophysical parameter value with the range of values that occur across the entire set of satellite observations. This can, for example, correct for the observational bias toward low *Kp* conditions. A half-orbit only lasts for ~50 min, so taking one value of the geomagnetic activity indices, *Kp* and *Dst*, for an individual half-orbit is adequate. Therefore in order to normalize the use of *Kp* or *Dst* data, the entire satellite data set is analyzed for equatorial crossings (when the satellite crosses the geographical equator) and a geomagnetic index value is recorded 1016 s after the equator crossing. This time delay is used so that the geomagnetic index value is taken when the satellite is at an absolute geographic subsatellite latitude of 59.3°, which is chosen because the average (absolute) database event geographic subsatellite latitude is 59.3°. Note that northward travelling orbits will have their geomagnetic index value taken when the geographic subsatellite latitude is at +59.3° (in the Northern Hemisphere) and southward travelling orbits at –59.3° (in the Southern Hemisphere). The end result of this normalization process is that we have one geomagnetic index value for every single half-orbit, which allows comparison of the PPAREP event geomagnetic index values with the normal occurrence of values in the entire set of satellite observations.

[28] Figure 6 (top panel) shows the resultant distribution of the detected events with respect to *Kp*. The results have been adjusted for the observational bias towards low *Kp* conditions in the same way as was described in detail for Figure 3, producing a normalized occurrence rate. This result provides very strong evidence that PPAREP events are more common during geomagnetic disturbances as identified by *Kp*. It shows that disturbances with *Kp* values > 4 are approximately three times more likely to produce a PPAREP event than periods with $Kp \sim 2$. The panel also shows that although *Kp* does have a significant relevance to the likelihood of an event occurring, there is not a lot of variance for the range $4 < Kp < 9$, and thus PPAREP is

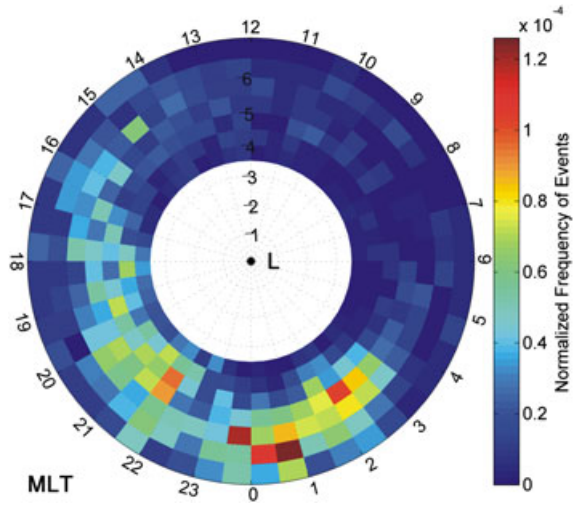

Figure 5. The distribution of events detected by IGRF *L*-value and MLT, where *L* increases from 0–7 R_e outward from the center. The majority of events are located near $L \sim 5$, and biased toward the evening and nighttime sectors.

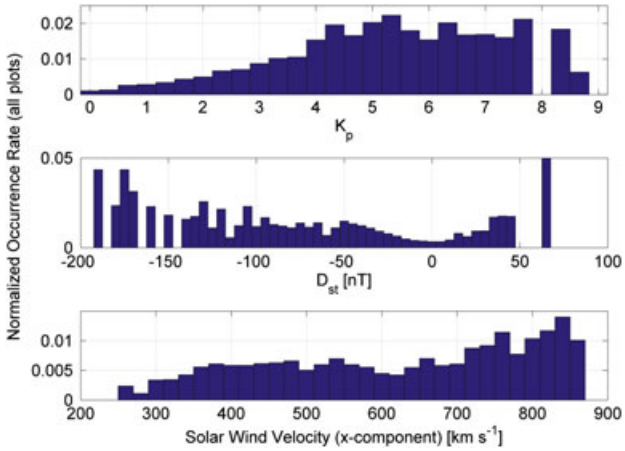

Figure 6. (top) The distribution of detected events with respect to *Kp*. The results have been adjusted for the observational bias toward low *Kp* conditions. (middle) The variation of normalized occurrence rate as a function of *Dst*. (bottom) The normalized occurrence rate as a function of solar wind speed. Note all plots in this figure share the same *x*-axes label of Normalized occurrence rate.

essentially equally common for all time periods with $Kp > 4$. Figure 6 (middle panel) shows the variation of normalized occurrence rate as a function of *Dst*. It is apparent that there is a gradual increase in the event activity rate as the *Dst* decreases from 0 to −50 nT. From −50 nT to −100 nT the activity rate is quite stable; however, below −100 nT it starts to vary more dramatically, most likely due to the small number of events in the sample at these very low values. There is also a noticeable peak for positive values of *Dst* from ~30–45 nT, which we speculate might correspond to a population of pressure pulse-driven EMIC waves, primarily near noon, producing these REP events.

[29] Finally, in Figure 6 (bottom panel), we plot the normalized occurrence rate as a function of solar wind speed. There are occasional gaps in the solar wind data availability; therefore, a check was performed to determine if the solar wind data value nearest to an event is more than one day away from the time that event occurred, if so, no solar wind value was recorded in the database. This process removed only 11 events from the total number available to be compared with solar wind velocity. The panel shows that there is a gradual increase in the event activity rate towards the highest velocities, suggesting that higher speed solar winds can increase the likelihood of an event, and produces approximately a factor of 3 change in occurrence frequency from low to high solar wind speeds.

[30] PPAREP events have previously been plotted in terms of *L*-shell. Underlying this distribution is the structure of the plasmasphere, with the location of the plasmapause being particularly relevant. The location of the plasmapause can be calculated with statistical plasmapause models, and we compare the results from two versions, *Moldwin et al*. [2002], which uses *Kp* (12 h maximum), and *O'Brien and Moldwin* [2003], which uses *Dst* (24 h minimum). Note that neither of these empirical plasmapause models explicitly contains a plasmaspheric drainage plume. Figure 7 shows a histogram of the difference of the *L*-shell of an event compared with the *L*-shell of the plasmapause reported by these statistical models. The top panel uses the *Moldwin et al*. [2002] *Kp*-driven plasmapause model, and the bottom panel uses the *O'Brien and Moldwin* [2003] *Dst*-driven model. Both panels indicate that 85–90% of the events are found outside of the plasmapause, and most commonly occur around +1 R_e beyond the statistical plasmapause location.

[31] To identify the REP events, we tested the factor of increase that any P6 0° channel spike had over the running mean at the same location. This was required to be at least a factor of three to cause an event trigger. Here we investigate if this factor of increase value is related to geomagnetic conditions. However, we note that while a large value in this parameter can represent a tall, narrow spike that has not significantly dragged the running mean up with it, it does not necessarily represent very strong REP with high fluxes if the running mean has been significantly influenced by the presence of the event. However, bearing this in mind this ratio parameter can still provide some insightful trends. We determined the mean *L*-shell and *Dst* values for PPAREP events falling inside a range of increase factors (3–5, 5–7, 7–9, 9–11, and 11–15) to see if there was a link between the increase factor and the *L*-shell or geomagnetic disturbance. Figure 8 (top panel) shows the mean factor of increase for each of the ranges against the mean *L*-value for the PPAREP events that fell in that range. Here we can see a trend suggesting larger factors of increase correspond with lower *L*-values. A similar analysis is shown in the bottom panel for *Dst*, which also suggests that larger factor of increase values correspond to lower values of *Dst* (and similarly for higher *Kp*—not shown).

[32] In order to analyze general overall event occurrence trends throughout the observation period, the events in the database were binned by year. As before, we performed normalization in order to remove the influence that the different launch dates of each satellite has on the event occurrence frequency. Figure 9 (top panel) shows an occurrence histogram of events by year from 1998–2010. The peak occurrence of events is in 2003, while the minimum is in 2009. The middle panel shows the daily sunspot number plotted against year over the same period. The peak sunspot number

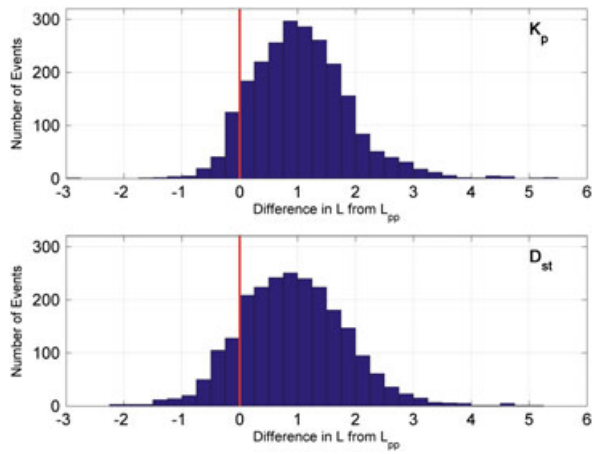

Figure 7. (top) A histogram of the difference of the IGRF *L*-shell of an event compared with the estimated *L*-shell of the plasmapause using the *Moldwin et al*. [2002] *Kp*-driven plasmapause model. (bottom) Similar histogram, but using the *O'Brien and Moldwin* [2003] *Dst*-driven model.

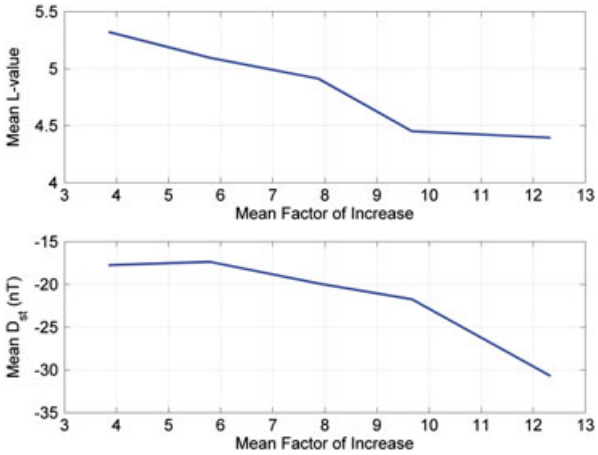

Figure 8. (top) The variation of the mean event IGRF *L*-value against the observed factor of increases seen in the EMIC REP events. The threshold of event detection is set at a factor of three. (bottom) The variation of *Dst* with the observed factor of increase.

is in 2000, and the minimum is 2008/9. There is no clear relationship between the event occurrence and solar cycle as represented by sunspot number. However, the bottom panel shows the smoothed geomagnetic activity index, *Ap*, plotted against year. The peak in *Ap* is in 2003, and the minimum is in 2009, which suggests that the variation in the occurrence of the REP events is more strongly influenced by geomagnetic activity than solar sunspot number. The panels show that events are more likely to occur during the declining phase of the solar cycle, which is when recurrent storms are prevalent [*Borovsky and Denton*, 2006]. Experimental observations indicate that EMIC wave power is present at geosynchronous orbit during high-speed solar wind stream periods, possibly driving REP at these times [*Fraser et al*., 2010].

5. Discussion

[33] We have investigated a database that was constructed containing the characteristics of 2331 REP events, and their associated parameters: *Kp*, *Dst*, and solar wind speed. Statistical analysis was then performed on this database to identify any trends between event occurrence and these parameters. The events were observed at *L*-values within the outer radiation belt ($3 < L < 7$) , were more common in the dusk and night sectors as determined by MLT, and were most common about +1 R_e outside of the plasmapause.

5.1. Comparison With REP Observations

[34] The PPAREP events detected in this study favor the dusk and nightside sectors. Other studies have also made observations of REP in the dusk and nighttime MLT sectors [*Imhof et al*., 1986; *Foat et al*., 1998; *Lorentzen et al*., 2000; *Millan et al*., 2002, 2010]. In particular, the use of polar orbiting satellites by *Imhof et al*. [1986] to investigate narrow relativistic electron precipitation spikes found that they occurred preferentially in the evening sector [*Imhof et al*., 1986, Figure 9]. They also found that approximately 31% of their 45 electron spikes occurred simultaneously with precipitation of >30 keV ions, with all 14 of these events associated with ion spikes occurring in the evening sector. *Millan et al*. [2002] used balloon observations of X-ray bursts to measure relativistic electron precipitation. They found nine events corresponding to precipitation of relativistic electrons with MeV energies, all of which occurred in the late afternoon and dusk sectors [*Millan et al*., 2002, Figure 5]. They suggested that scattering by EMIC waves was a likely mechanism for the precipitation observed. Examples of EMIC driven REP has also been reported through ground-based data [*Rodger et al*., 2008] and a combination of ground and spacecraft data [*Miyoshi et al*., 2008], both of which are detailed in the next subsection. However, at this point we are unaware of any large statistical study focused on the characteristics of EMIC wave driven REP preceding the current paper.

5.2. Comparison With EMIC Waves

[35] *Engebretson et al*. [2008] investigated two geomagnetic storms that occurred during 2005 using a combination of Antarctic-based magnetometers and riometers, as well as the POES spacecraft. Magnetometers at three locations (Halley, South Pole Station, and McMurdo) were used to identify Pc1 wave activity. Comparison of the events in our database with the storm periods of 18–19 July 2005 and 24–27 August 2005 revealed four detected REP events in these timeframes. Three of the four events were matched to observations of Pc1 waves in the magnetometer data, with the fourth occurring during broadband ULF noise. *Engebretson et al*. [2008] suggested that because the ULF spectral patterns appeared identical for all three stations the wave power had been ducted horizontally through the ionospheric waveguide to the three magnetometers, and the exact location of the flux tube could not

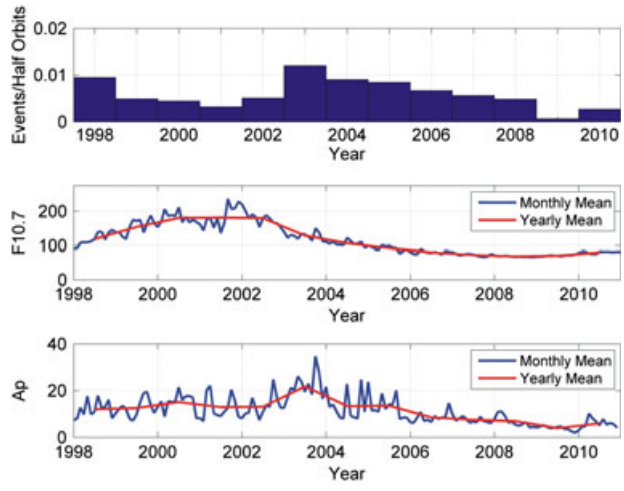

Figure 9. (top) An occurrence frequency histogram of events by year from 1998–2010. The peak occurrence of events is in 2003, while the minimum is in 2009. (middle) The sunspot number (monthly mean and yearly mean) plotted against year over the same period. The peak sunspot number is in 2001, and the minimum is 2008/9. (bottom) The smoothed geomagnetic activity index, *Ap*, plotted against year. The peak in *Ap* occurs in 2003, and the minimum occurs in 2009, which is similar to the occurrence of events shown in the top panel.

be exactly determined. The PPAREP event in our database, detected at 07:55 UT by NOAA-16 on 27 August 2005, corresponds with the timing of the Pc1 observations shown in *Engebretson et al*. [2008, Figure 4]. The *L*-value for our event corresponds best with Halley, which was also the station that showed the highest intensity waves. Our analysis also detected events on 19 July 2005 (NOAA-16) and 25 August 2005 (NOAA-18) that corresponded with reported Pc1 observations in the Engebretson et al. study.

[36] *Rodger et al*. [2008] used entirely ground-based systems to combine EMIC observations provided by a chain of pulsation magnetometers with energetic electron precipitation observed by a subionospheric VLF receiver and a chain of riometers. The magnetometers and riometers were located throughout Finland. The VLF propagation paths utilized were between transmitters in Anthorn, UK and Keflavik, Iceland, and a receiver in Sodankylä, Finland. Their study identified four events in which precipitation was detected using the VLF propagation paths, while the riometers showed little absorption, suggesting precipitation of relativistic (~1 MeV) electrons. Simultaneous EMIC observations were made during this time period with the magnetometers, linking EMIC waves to the precipitation observed. All of the events occurred during the MLT dusk sector. Analysis of our REP database revealed that one of the four Rodger et al. events had a corresponding close match with our MEPED-reported PPAREP events. This particular event occurred on 22 November 2007, 1630–1700 UT. Our database matched two potential PPAREP events to this timeframe, occurring at 16:01 UT and 17:42 UT. Both of our events were observed by NOAA-16, with subsatellite geographical locations between Greenland and Europe.

[37] *Miyoshi et al*. [2008] investigated REP occurring on 5 September 2005. At ~04:59 UT they observed an isolated proton aurora at Athabasca, Canada, while simultaneously recording magnetic pulsations using an induction magnetometer also located at Athabasca. They determined that these pulsations were helium-band EMIC waves. In order to match these ground observations with satellite-based particle observations, they made use of NOAA-17, which passed over Athabasca during this time. The MEPED data showed an isolated peak of precipitating protons with energies of tens of keV in the P1 0° channel. This was then matched to simultaneous precipitating electrons with energies "$>$800 keV" (from the P6 0° channel) and "$>$3 MeV" (from the P6 omnidirectional detector). The pass reported by Miyoshi using NOAA-17 did not produce an event in our PPAREP event database. However, closer investigation shows that although the P1 0° channel does trigger, there is not a sufficient ratio of increase in the P6 0° channel over the running mean to also trigger, and hence lead to the identification of an event. While the NOAA-17 pass did not fulfill our criteria as required to be identified as a PPAREP event, analysis of our event database reveals that NOAA-15 detected an event at 04:48 UT, only 11 min before the Miyoshi NOAA-17 pass, well within the window of 02:30–08:00 UT that the pulsations were observed with the magnetometer at Athabasca and the 04:30–05:00 UT auroral image window found from the observed emission profile of the Hydrogen Balmer line. Furthermore, the event detected by NOAA-15 occurs only 0.23° latitude and 1.56° longitude away from the Southern Hemisphere conjugate location of the NOAA-17 proton spike. In comparison with the NOAA-17 pass, the NOAA-15 conjugate event shows a much stronger response, with very obvious large sharp spikes, in both the P1 0° and P6 0° channels.

[38] Thus, the comparison with known EMIC wave events suggests that the PPAREP events detected in our database are EMIC-driven REP events. However, it is important to note that studies into the statistical occurrence of EMIC waves show peak occurrence rates in different MLT sectors than we find for our events (Figure 5), which were more common in the dusk and night sectors. Multiple space-based studies using different satellites have concluded that EMIC waves are most common near noon and in the dusk sector for the *L*-shell range, which overlaps with the outer radiation belts [e.g., *Anderson et al*., 1992; *Halford et al*., 2010; *Clausen et al*., 2011], i.e., approximately 6 MLT earlier than seen in our PPAREP events. Ground-based statistical studies show similar occurrence locations to the satellite studies. When these wave statistics are incorporated into global physics-based models they drive low-energy proton and relativistic electron precipitation in the noon and dusk sectors [e.g., *Jordanova et al*., 2008], rather than the sectors shown in Figure 5. Nonetheless, we note that the precipitation events selected were found using the expected particle precipitation signature caused by EMIC waves (low-energy protons and high-energy electrons). The subset of PPAREP events that peak at ~2 MLT do not agree well with either ground or satellite EMIC wave occurrence statistics reported in the literature. It is known that REP events can be due to scattering from waves other than EMIC, such as VLF whistler mode waves. Chorus and Hiss can produce radiation belt electron loss, and are more likely to be found on the nightside [*Summers et al*., 2007]. However, VLF waves, while able to scatter energetic electrons, are not resonant with protons, and it is unclear that they could therefore produce REP events that would be detected using the algorithm applied here, i.e., VLF waves alone are unable to produce PPAREP events. Given the strong disagreement between the observed EMIC-wave distribution and the distribution of PPAREP events, one can speculate that other drivers may be causing our observed precipitation for $L > 6$. For example substorms are known to lead to enhanced proton precipitation [*Gvozdevsky et al*., 1997] and cause REP [*Clilverd et al*., 2008, 2012], although we are not aware that the precipitation drivers during substorms expected to produce near-simultaneous narrow spikes in protons and relativistic electrons.

5.3. Comparison With Proton Precipitation Events

[39] *Sandanger et al*. [2009] analyzed the location of proton precipitation spikes occurring within the anisotropic proton zone during three case-study storm periods. A proton precipitation spike is described as a localized burst of precipitating and locally trapped 30–80 keV protons so strong as to generate isotropic proton precipitation within the anisotropic proton zone [*Sandanger et al*., 2009, Figure 9]. The proton precipitation spikes fulfill some of the criteria to be defined as a PPAREP event in the current paper; however, they did not also require the simultaneous spike in the P6 (relativistic electrons) channel. Therefore, the events investigated in this current work are likely to form a subset of the proton

precipitation spikes investigated by *Sandanger et al*. [2009]. For the three storms they studied 88%, 96%, and 93% of the spikes were found to be located inside the plasmapause. Examination of our PPAREP event database found six events that occurred within the Sandanger et al. storm periods. All events were from NOAA-15 as no other satellites used in our study (i.e., SEM-2 instrumented) were in orbit during the time periods investigated. The pre-NOAA-15 satellites that *Sandanger et al*. [2009] used were not carrying the SEM-2 instrument package (for example NOAA-12). All six Sandanger proton precipitation spikes that matched with our detected PPAREP events occurred either outside the plasmapause, or very close to it. We have also shown that the majority of our PPAREP events occur outside of the plasmapause, while *Sandanger et al*. [2009] found that the generalized proton precipitation spikes almost entirely occur inside the plasmapause, but both can be driven by EMIC waves. Thus, the comparison suggests that only a subset of EMIC-driven proton precipitation events simultaneously produce relativistic electron precipitation, and only when conditions outside the plasmapause are favorable.

5.4. Comparison With Plasmaspheric Plumes

[40] Many studies have suggested a link between EMIC waves in plasmaspheric plumes and proton precipitation [*Spasojevic et al*., 2004; *Jordanova et al*., 2007; *Yahnina et al*., 2008; *Spasojevic and Fuselier*, 2009; *Yuan et al*., 2010; *Usanova et al*., 2010; *Spasojevic et al*., 2011] as well as REP [e.g., *Chen et al*., 2009]. *Darrouzet et al*. [2008] performed a large statistical analysis of plasmaspheric plumes using a database of 5 yr worth of Cluster observations. While Figure 8 of *Darrouzet et al*. [2008] shows peak plume occurrence in the late afternoon sector around 16 MLT and $L > 7$, our events favor the dusk-midnight sector, with highest occurrence rates around 00 MLT and $L > 5$. This strongly suggests that any potential correlation between our PPAREP events and plasmaspheric plumes is not related to plume frequency rates. In addition, *Darrouzet et al*. [2006] listed some case study events where individual plume information was presented, as well as Cluster and IMAGE observations; however, there is no coincidence between the three events listed and our PPAREP events.

6. Summary and Conclusions

[41] Using six satellites carrying the SEM-2 instrument package, a total 436,422 individual half-orbits between 1998 and 2010 were inspected by an automatic detection algorithm searching for EMIC-driven relativistic electron precipitation. The algorithm searched for one of the key characteristics of EMIC-driven REP, identified as the simultaneity between the P1 (52 keV differential proton flux channel) and P6 (>800 keV electron channel) spikes. In all, 2331 events were identified as showing sudden spikes in relativistic electron precipitation as well as proton precipitation. Care was taken to ensure the identified results were of high quality and reduce the number of false triggers, at the risk of missing true events. A database was constructed containing all proton precipitation associated REP (PPAREP) events, and other geomagnetic parameters such as *Kp*, *Dst*, solar wind data, and statistical plasmapause location model values were also included. Statistical analysis was then performed on this database to identify any trends between event occurrence and these parameters.

[42] The events were observed at *L*-values within the outer radiation belt ($3 < L < 7$) and were more common in the dusk and night sectors as determined by MLT, which agrees well with the known distribution of EMIC waves. However, the majority of the PPAREP events occurred in the midnight/dawn sector, unlike the known EMIC-wave distributions. Comparison with three studies in the literature, which made direct observations of EMIC waves, show evidence that the events identified in this study are likely to be EMIC-driven REP, with further evidence coming from a different study that looked at proton precipitation likely produced by EMIC waves. When we observed REP events during the periods examined in the three published papers, our REP events showed good correlation both in time and location with the EMIC waves. However, we did not observe REP events for all the EMIC waves reported in those studies. The majority of events are observed to occur outside the plasmasphere at *L*-values greater than plasmapause locations as determined from statistical models. The events make up a subset of the proton spikes investigated by *Sandanger et al*. [2009], and potentially reflect different overall characteristics than these proton spikes, particularly when comparing their location to that of the plasmapause, i.e., proton precipitation inside the plasmapause, and REP outside the plasmapause. There was no clear relationship identified between the expected typical location of plasmaspheric plumes and the locations of the PPAREP events detected.

[43] Analysis of the PPAREP event occurrence compared with *Kp*, *Dst*, and solar wind speed showed that high solar wind speed, and geomagnetic storms increase the likelihood of an event being detected. A link with solar cycle activity levels was also shown, with low geomagnetic activity leading to a low event detection rates, and the peak occurrence occurring during the declining phase of the solar cycle, consistent with the 2003 maximum in geomagnetic activity index, *Ap*. The "strength" of the electron precipitation spike was tied to geomagnetic disturbances, with stronger storms producing relatively larger spikes. However, care should be taken when using this result as it may be influenced by the way it was estimated using a running mean.

[44] This study has generated the largest known database of likely EMIC-driven REP events, providing insight into trends and associations that cannot easily be identified by investigating individual geomagnetic storms. As noted above, the identification of the EMIC-driven REP events has relied upon the expected pitch angle scattering by EMIC waves of relativistic electrons and comparatively low-energy protons. For the vast majority of the events detected we have not confirmed the existence of EMIC waves at this time, and hence it is possible that some of the REP events reported might be false positives and not caused by EMIC waves, particularly those events that were detected just after MLT midnight. We are currently planning future studies to investigate the conjunctions of these events with EMIC wave observations.

[45] **Acknowledgments.** The research leading to these results has received funding from the European Union Seventh Framework Programme [FP7/2007-2013] under grant agreement n°263218. The authors would like to thank the researchers and engineers of NOAA's Space Environment

Centre for the provision of the data and the operation of the SEM-2 instrument carried onboard these spacecraft.

References

Anderson, B. J., R. E. Erlandson, and L. J. Zanetti (1992), A Statistical Study of Pc 1-2 Magnetic Pulsations in the Equatorial Magnetosphere, 1. Equatorial Occurrence Distributions, *J. Geophys. Res.*, *97*(A3), 3075–3088, doi:10.1029/91JA02706.

Anderson, B. J. (1995), Proton cyclotron wave-ion interactions observed by AMPTE/CCE, in Cross-Scale Coupling in Space Plasmas, *Geophys. Monogr. Ser*., vol. 93, edited by L. Horwitz, N. Singh, and L. Burch, pp. 193–200, AGU, Washington, D. C., doi:10.1029/GM093p0193.

Borovsky, J. E., and M. H. Denton (2006), Differences between CME-driven storms and CIR-driven storms, *J. Geophys. Res.*, *111*, A07S08, doi:10.1029/2005JA011447.

Bortnik, J., J. W. Cutler, C. Dunson, T. E. Bleier, and R. L. McPherron (2008), Characteristics of low-latitude Pc1 pulsations during geomagnetic storms, *J. Geophys. Res.*, *113*(A4), doi:10.1029/2007JA012867.

Brasseur, G. P., and S. Solomon (2005), Aeronomy of the Middle Atmosphere, 3rd revised and enlarged ed., Springer, Dordrecht.

Chen, L., R. M. Thorne, and R. B. Horne (2009), Simulation of EMIC wave excitation in a model magnetosphere including structured high-density plumes, *J. Geophys. Res.*, *114*, A07221, doi:10.1029/2009JA014204.

Clausen, L. B. N., J. B. H. Baker, J. M. Ruohoniemi, and H. J. Singer (2011), EMIC waves observed at geosynchronous orbit during solar minimum: Statistics and excitation, *J. Geophys. Res.*, *116*, A10205, doi:10.1029/2011JA016823.

Clilverd, M. A., C. J. Rodger, J. B. Brundell, N. Cobbett, J. Bähr, T. Moffat-Griffin, A. J. Kavanagh, A. Seppälä, N. R. Thomson, R. H. W. Friedel, and F. W. Menk, (2008), Energetic electron precipitation during sub-storm injection events: high latitude fluxes and an unexpected mid-latitude signature, *J. Geophys. Res.*, *113*, A10311, doi:10.1029/2008JA013220.

Clilverd, M. A., C. J. Rodger, I. J. Rae, J. B. Brundell, N. R. Thomson, N. Cobbett, P. T. Verronen, and F. W. Menk, (2012), Combined THEMIS and ground-based observations of a pair of substorm associated electron precipitation events, *J. Geophys. Res.*, *117*, A02313, doi:10.1029/2011ja016933.

Cornwall, J. M. (1965), Cyclotron Instabilities and Electromagnetic Emission in the Ultra Low Frequency and Very Low Frequency Ranges, *J. Geophys. Res.*, *70*(1), 61–69, doi:10.1029/JZ070i001p00061.

Darrouzet, F., et al. (2006), Analysis of plasmaspheric plumes: CLUSTER and IMAGE observations, *Annales Geophysicae*, *24*, 1737–1758, doi:10.5194/angeo-24-1737-2006.

Darrouzet, F., J. de Keyser, P. Décréau, F. El Lemdani-Mazouz, and X. Vallières (2008), Statistical analysis of plasmaspheric plumes with Cluster/WHISPER observations, *Annales Geophysicae*, *26*, 2403–2417, doi:10.5194/angeo-26-2403-2008.

Engebretson, M. J., et al. (2008), Pc1-Pc2 waves and energetic particle precipitation during and after magnetic storms: Superposed epoch analysis and case studies, *J. Geophys. Res.*, *113*(A1), doi:10.1029/2007JA012362.

Erlandson, R. E., and A. J. Ukhorskiy (2001), Observations of electromagnetic ion cyclotron waves during geomagnetic storms: Wave occurrence and pitch angle scattering, *J. Geophys. Res.*, *106*(A3), 3883–3895, doi:10.1029/2000JA000083.

Evans, D. S., and M. Greer (2000), Polar Orbiting Environmental Satellite Space Environment Monitor - 2 Instrument Descriptions and Archive Data Documentation, Tech. rep., National Atmospheric and Oceanic Administration.

Evans, D., H. Garrett, I. Jun, R. Evans, and J. Chow (2008), Long-term observations of the trapped high-energy proton population ($L < 4$) by the NOAA Polar Orbiting Environmental Satellites (POES), *Advances in Space Research*, *41*(8), 1261–1268.

Foat, J. E., et al. (1998), First detection of a terrestrial MeV X-ray burst, *Geophys. Res. Lett.*, *25*(22), 4109–4112, doi:10.1029/1998GL900134.

Fraser, B. J., T. M. Loto'aniu, and H. J. Singer (2006), Electromagnetic Ion Cyclotron Waves in the Magnetosphere, Washington DC American Geophysical Union Geophysical Monograph Series, 169, 195.

Fraser, B., and T. Nguyen (2001), Is the plasmapause a preferred source region of electromagnetic ion cyclotron waves in the magnetosphere?, *Journal of Atmospheric and Solar-Terrestrial Physics*, *63*(11), 1225–1247, doi:10.1016/S1364-6826(00)00225-X.

Fraser, B. J., R. S. Grew, S. K. Morley, J. C. Green, H. J. Singer, T. M. Loto'aniu, and M. F. Thomsen (2010), Storm time observations of electromagnetic ion cyclotron waves at geosynchronous orbit: GOES results, *J. Geophys. Res.*, *115*, A05208, doi:10.1029/2009JA014516.

Fraser, B. J., H. J. Singer, M. L. Adrian, D. L. Gallagher, and M. F. Thomsen (2005), The relationship between plasma density structure and EMIC waves at geosynchronous orbit, in Inner Magnetosphere Interactions: New Perspectives From Imaging, *Geophys. Monogr. Ser*., vol. 159, edited by J. Burch, M. Schulz, and H. Spence, pp. 55–70, AGU, Washington, D. C., doi:10.1029/159GM04.

Gvozdevsky, B. B., V. A. Sergeev, and K. Mursula (1997), Long lasting energetic proton precipitation in the inner magnetosphere after substorms, *J. Geophys. Res.*, *102*(A11), 24,333–24,338, doi:10.1029/97JA02062.

Halford, A. J., B. J. Fraser, and S. K. Morley (2010), EMIC wave activity during geomagnetic storm and nonstorm periods: CRRES results, *J. Geophys. Res.*, *115*(A12), doi:10.1029/2010JA015716.

Horne, R. B., M. M. Lam, and J. C. Green (2009), Energetic electron precipitation from the outer radiation belt during geomagnetic storms, *Geophys. Res. Lett.*, *36*(19), doi:10.1029/2009GL040236.

Imhof, W. L., H. D. Voss, J. B. Reagan, D. W. Datlowe, E. E. Gaines, J. Mobilia, and D. S. Evans (1986), Relativistic Electron and Energetic Ion Precipitation Spikes Near the Plasmapause, *J. Geophys. Res.*, *91*(A3), 3077–3088, doi:10.1029/JA091iA03p03077.

Jordanova, V. K., M. Spasojevic, and M. F. Thomsen (2007), Modeling the electromagnetic ion cyclotron wave-induced formation of detached subauroral proton arcs, *J. Geophys. Res.*, *112*(A8), doi:10.1029/2006JA012215.

Jordanova, V. K., J. Albert, and Y. Miyoshi (2008), Relativistic electron precipitation by EMIC waves from self-consistent global simulations, *J. Geophys. Res.*, *113*, A00A10, doi:10.1029/2008JA013239.

Lorentzen, K. R., M. P. McCarthy, G. K. Parks, J. E. Foat, R. M. Millan, D. M. Smith, R. P. Lin, and J. P. Treilhou (2000), Precipitation of relativistic electrons by interaction with electromagnetic ion cyclotron waves, *J. Geophys. Res.*, *105*(A3), 5381–5389, doi:10.1029/1999JA000283.

Lyons, L. R., and R. M. Thorne (1972), Parasitic pitch angle diffusion of radiation belt particles by ions cyclotron waves, *J. Geophys. Res.*, *77*, 5608–5617.

Meredith, N. P., R. M. Thorne, R. B. Horne, D. Summers, B. J. Fraser, and R. R. Anderson (2003), Statistical analysis of relativistic electron energies for cyclotron resonance with EMIC waves observed on CRRES, *J. Geophys. Res.*, *108*(A6), doi:10.1029/2002JA009700.

Millan, R. M., and R. M. Thorne (2007), Review of radiation belt relativistic electron loss, *J. Atmos. Sol. Terr. Phys.*, *69*, 362–377, doi:10.1016/j.jastp.2006.06.019.

Millan, R. M., K. B. Yando, J. C. Green, and A. Y. Ukhorskiy (2010), Spatial distribution of relativistic electron precipitation during a radiation belt depletion event, *Geophys. Res. Lett.*, *37*(20), doi:10.1029/2010GL044919.

Millan, R. M., R. P. Lin, D. M. Smith, K. R. Lorentzen, and M. P. McCarthy (2002), Xray observations of MeV electron precipitation with a balloon-borne germanium spectrometer, *Geophys. Res. Lett.*, *29*(24), doi:10.1029/2002GL015922.

Miyoshi, Y., K. Sakaguchi, K. Shiokawa, D. Evans, J. Albert, M. Connors, and V. Jordanova (2008), Precipitation of radiation belt electrons by EMIC waves, observed from ground and space, *Geophys. Res. Lett.*, *35*(23), doi:10.1029/2008GL035727.

Moldwin, M. B., L. Downward, H. K. Rassoul, R. Amin, and R. R. Anderson (2002), A new model of the location of the plasmapause: CRRES results, *J. Geophys. Res.*, *107*(A11), doi:10.1029/2001JA009211.

O'Brien, T. P., and M. B. Moldwin (2003), Empirical plasmapause models from magnetic indices, *Geophys. Res. Lett.*, *30*(4), doi:10.1029/2002GL016007.

Pickett, J. S., et al. (2010), Cluster observations of EMIC triggered emissions in association with Pc1 waves near Earth's plasmapause, *Geophys. Res. Lett.*, *37*(9), doi:10.1029/2010GL042648.

Posch, J. L., M. J. Engebretson, M. T. Murphy, M. H. Denton, M. R. Lessard, and R. B. Horne (2010), Probing the relationship between electromagnetic ion cyclotron waves and plasmaspheric plumes near geosynchronous orbit, *J. Geophys. Res.*, *115*, A11205, doi:10.1029/2010JA015446.

Reeves, G. D., K. L. McAdams, R. H. W. Friedel, and T. P. O'Brien (2003), Acceleration and loss of relativistic electrons during geomagnetic storms, *Geophys. Res. Lett.*, *30*(10), doi:10.1029/2002GL016513.

Robel, J. (Ed.), (2009), NOAA KLM User's Guide, National Environmental Satellite, Data, and Information Service.

Rodger, C. J., B. R. Carson, S. A. Cummer, R. J. Gamble, M. A. Clilverd, J. C. Green, J.-A. Sauvaud, M. Parrot, and J.-J. Berthelier (2010a), Contrasting the efficiency of radiation belt losses caused by ducted and non-ducted whistlermode waves from ground-based transmitters, *J. Geophys. Res.*, *115*(A12), doi:10.1029/2010JA015880.

Rodger, C. J., M. A. Clilverd, J. C. Green, and M. M. Lam (2010b), Use of POES SEM-2 observations to examine radiation belt dynamics and energetic electron precipitation into the atmosphere, *J. Geophys. Res.*, *115*(A4), doi:10.1029/2008JA014023.

Rodger, C. J., T. Raita, M. A. Clilverd, A. Seppälä, S. Dietrich, N. R. Thomson, and T. Ulich (2008), Observations of relativistic electron precipitation from the radiation belts driven by EMIC waves, *Geophys. Res. Lett.*, *35*(16), doi:10.1029/2008GL034804.

Sandanger, M., F. Søraas, K. Aarsnes, K. Oksavik, and D. S. Evans (2007), Loss of relativistic electrons: Evidence for pitch angle scattering by

electromagnetic ion cyclotron waves excited by unstable ring current protons, *J. Geophys. Res.*, *112*(A12), doi:10.1029/2006JA012138.

Sandanger, M., F. Søraas, M. Sørbø, K. Aarsnes, K. Oksavik, and D. Evans (2009), Relativistic electron losses related to EMIC waves during CIR and CME storms, *Journal of Atmospheric and Solar-Terrestrial Physics*, *71*(10-11), 1126–1144, doi:10.1016/j.jastp.2008.07.006.

Søraas, F., K. Aarsnes, D. Carlsen, K. Oksavik, and D. Evans (2005), Ring Current Behavior as Revealed by Energetic Proton Precipitation, Washington DC American Geophysical Union Geophysical Monograph Series, 155, 237.

Spasojevic, M., H. U. Frey, M. F. Thomsen, S. A. Fuselier, S. P. Gary, B. R. Sandel, and U. S. Inan (2004), The link between a detached subauroral proton arc and a plasmaspheric plume, *Geophys. Res. Lett.*, *31*(4), doi:10.1029/2003GL018389.

Spasojevic, M., and S. A. Fuselier (2009), Temporal evolution of proton precipitation associated with the plasmaspheric plume, *J. Geophys. Res.*, *114*(A12), doi:10.1029/2009JA014530.

Spasojevic, M., L. W. Blum, E. A. MacDonald, S. A. Fuselier, and D. I. Golden (2011), Correspondence between a plasma-based EMIC wave proxy and subauroral proton precipitation, *Geophys. Res. Lett.*, *38*(23), doi:10.1029/2011GL049735.

Summers, D., and R. M. Thorne (2003), Relativistic electron pitch-angle scattering by electromagnetic ion cyclotron waves during geomagnetic storms, *J. Geophys. Res.*, *108*(A4), 1143, doi:10.1029/2002JA009489.

Summers, D., B. Ni, and N. P. Meredith (2007), Timescales for radiation belt electron acceleration and loss due to resonant wave-particle interactions: 2. Evaluation for VLF chorus, ELF hiss, and electromagnetic ion cyclotron waves, *J. Geophys. Res.*, *112*, A04207, doi:10.1029/2006JA011993.

Tsurutani, B. T., and G. S. Lakhina (1997), Some basic concepts of wave-particle interactions in collisionless plasmas, *Rev. Geophys.*, *35*(4), 491–501, doi:10.1029/97RG02200.

Usanova, M. E., et al. (2010), Conjugate ground and multisatellite observations of compression-related EMIC Pc1 waves and associated proton precipitation, *J. Geophys. Res.*, *115*(A7), doi:10.1029/2009JA014935.

Usanova, M. E., I. R. Mann, I. J. Rae, Z. C. Kale, V. Angelopoulos, J. W. Bonnell, K. H. Glassmeier, H. U. Auster, and H. J. Singer (2008), Multipoint observations of magnetospheric compression-related EMIC Pc1 waves by THEMIS and CARISMA, *Geophys. Res. Lett.*, *35*(17), doi:10.1029/2008GL034458.

Yahnina, T. A., H. U. Frey, T. Bösinger, and A. G. Yahnin (2008), Evidence for subauroral proton flashes on the dayside as the result of the ion cyclotron interaction, *J. Geophys. Res.*, *113*(A7), doi:10.1029/2008JA013099.

Yando, K., R. M. Millan, J. C. Green, and D. S. Evans (2011), A Monte Carlo simulation of the NOAA POES Medium Energy Proton and Electron Detector instrument, *J. Geophys. Res.*, *116*(A10), doi:10.1029/2011JA016671.

Yuan, Z., et al. (2010), Link between EMIC waves in a plasmaspheric plume and a detached sub-auroral proton arc with observations of Cluster and IMAGE satellites, *Geophys. Res. Lett.*, *37*(7), doi:10.1029/2010GL042711.